International Journal of Multiphase Flow 68 (2015) 121–134

Contents lists available at ScienceDirect

International Journal of Multiphase Flow

journal homepage: www.elsevier.com/locate/ijmulflow

Large Eddy Simulation and theoretical investigations of the transient cavitating vortical flow structure around a NACA66 hydrofoil

B. Ji [a], X.W. Luo [a,*], Roger E.A. Arndt [b], Xiaoxing Peng [c], Yulin Wu [a]

[a] State Key Laboratory of Hydroscience & Engineering, Tsinghua University, Beijing 100084, China
[b] Saint Anthony Falls Laboratory, University of Minnesota, Minneapolis, MN 55414, USA
[c] China Ship Scientific Research Center, Wuxi 214082, China

ARTICLE INFO

Article history:
Received 10 July 2014
Received in revised form 17 October 2014
Accepted 20 October 2014
Available online 25 October 2014

Keywords:
Sheet/cloud cavitation
Large Eddy Simulation (LES)
Vortex structures
Vorticity transport equation
One-dimensional model
Cavity volume acceleration

ABSTRACT

Compared to non-cavitating flow, cavitating flow is much complex owing to the numerical difficulties caused by cavity generation and collapse. In this paper, the cavitating flow around a NACA66 hydrofoil is studied numerically with particular emphasis on understanding the cavitation structures and the shedding dynamics. Large Eddy Simulation (LES) was coupled with a homogeneous cavitation model to calculate the pressure, velocity, vapor volume fraction and vorticity around the hydrofoil. The predicted cavitation shedding dynamics behavior, including the cavity growth, break-off and collapse downstream, agrees fairly well with experiment. Some fundamental issues such as the transition of a cavitating flow structure from 2D to 3D associated with cavitation–vortex interaction are discussed using the vorticity transport equation for variable density flow. A simplified one-dimensional model for the present configuration is adopted and calibrated against the LES results to better clarify the physical mechanism for the cavitation induced pressure fluctuations. The results verify the relationship between pressure fluctuations and the cavity shedding process (e.g. the variations of the flow rate and cavity volume) and demonstrate that the cavity volume acceleration is the main source of the pressure fluctuations around the cavitating hydrofoil. This research provides a better understanding of the mechanism driving the cavitation excited pressure pulsations, which will facilitate development of engineering designs to control these vibrations.

Introduction

Owing to it's importance in a wide range of fundamental studies and engineering applications, much effort has been made in the past decades to study cavitation shedding dynamics. Sheet cavitation shedding often leads to cloud cavitation, which strongly affects hydrodynamic performance and produces vibration, noise and cavitation erosion. Comprehensive reviews on this subject have been given in the literature, e.g. Arndt, 1981, 2002; Brennen, 1995; Franc and Michel, 2005. These reviews outline the significant progress that has been made in the development of the tools necessary to carry out this research.

In the past, numerous experiments have been conducted to study partial cavitation structures especially on hydrofoils (Astolfi et al., 2000; Reisman et al., 1998; Tassin et al., 1995; Wang et al., 2001) or in Venturi-type sections (Barre et al., 2009; Stutz and Reboud, 1997a,b). These experiments showed that partial sheet cavities are periodically broken-up and rolled up into bubble clouds. Although many interesting studies have been reported on these physical mechanisms, they are not yet fully understood due to the complex features of partial cavitating flows such as bubbly flow, laminar transition or turbulent flows, detached and reattached flows, shear layers and vortical structures. Kubota et al. (1989) successfully measured the unsteady structure of cloud cavitation using Laser Doppler Anemometry (LDA) and matched the measurements with unsteady cavities photographed by a high-speed camera. Their results showed that the cloud cavitation observed in the experiment had a vorticity maximum at its center and a cluster containing many small cavitation bubbles. The structure of the two-phase flow inside the cavity was investigated by Stutz and Reboud (1997a,b). They succeeded in measuring the local void fraction and the velocity inside the cavities and confirmed the existence of reversed two-phase flow along the wall. Foeth (2008), Foeth et al. (2006) and Foeth et al. (2008) used time-resolved PIV and a high speed camera to study fully developed sheet cavitation

* Corresponding author. Tel./fax: +86 10 62789853.
E-mail addresses: jibin@mail.tsinghua.edu.cn (B. Ji), luoxw@mail.tsinghua.edu.cn (X.W. Luo), arndt001@umn.edu (R.E.A. Arndt), henrypxx@163.com (X. Peng), wyl-dhh@mail.tsinghua.edu.cn (Y. Wu).

http://dx.doi.org/10.1016/j.ijmultiphaseflow.2014.10.008
0301-9322/

on a hydrofoil with a spanwise varying angle of attack and clarified that the shedding of a sheet cavity was governed by the direction and momentum of re-entrant and side-entrant jets and their impingement on the free surface of the cavity, which has been confirmed by numerical simulation (Ji et al., 2013b; Park and Rhee, 2013). Le et al. (1993) studied the global behavior of partial cavities, including the cavitation patterns, cavity length, periodic shedding, and mean pressure in the cavity closure region. They found that the cavity unsteadiness is intimately related to the cavity thickness and the re-entrant jet is associated with vorticity production. Reliable estimates of the shedding rate of the circulation by the re-entrant jet mechanism for a periodic cavity were obtained. Kawanami et al. (1997) thoroughly investigated cloud cavitation in a series of detailed experiments on a two-dimensional Elliptic Nose Foil with high-speed photography as well as with pressure measurements utilizing surface mounted pressure transducers and a hydrophone. They established a clear relationship between the re-entrant jet and the cloud cavity generation process. They then pointed out that a small obstacle attached at the mid-span near the termination of the sheet cavity can block the re-entrant jet, thereby preventing the generation of the cloud cavity. Pham et al. (1999) also conducted an experimental investigation of unsteady sheet cavitation using non-intrusive techniques to study the re-entrant jet dynamics and the interfacial instabilities. They found that the frequencies of re-entrant jet surges are equal to the cloud shedding frequencies determined by unsteady pressure measurements, which demonstrated that the cloud shedding is actually driven by the re-entrant jet. Analysis of gravity effect showed that the re-entrant jet role predominates over the interfacial instabilities in the generation of periodic cloud shedding. Arndt et al. (2000) used a two-dimensional NACA0015 hydrofoil to investigate the complex physics involved in the transition of sheet cavitation to cloud cavitation with an integrated experimental/numerical approach. They indicated that two competing mechanisms are found for the induced shedding of cloud cavitation. At high values of $\sigma/2\alpha$, the re-entrant jet physics dominate, while at low values of $\sigma/2\alpha$, bubbly flow shock wave phenomena dominate. Watanabe et al. (2001) used a linearized free streamline theory employing a singularity method to show that when the re-entrant jet is not taken into account, cavitation instability originates from the transitional cavity oscillation and the transition between partial and super cavities. Callenaere et al. (2001) experimentally investigated the instability of a partial cavity induced by the development of a re-entrant jet on a diverging step. They argued that the two parameters having the greatest effect on the re-entrant instability are: the adverse pressure gradient and the cavity thickness compared to the re-entrant jet thickness. Laberteaux and Ceccio (2001) observed two types of partial cavities with closed partial cavities formed on a two dimensional NACA0009 hydrofoil and open partial cavities without re-entrant flow formed on a plano-convex hydrofoil. High-speed observation and PIV measurements of cavitating flows around a semi-circular leading-edge flat plate and NACA0015 hydrofoil was recently reported by Kravtsova et al. (2014). Their results show that cavitation inception is governed by the development of the carrier-fluid flow around the foil leading edges, but the subsequent flow pattern depends strongly on the cavitation regime displaying markedly different distributions compared to the non-cavitating case.

The various limitations of measurement techniques have resulted in noticeable efforts to use numerical simulations of cavitating flows in recent years. Many cavitation models have been based on the assumption of a homogenous equilibrium medium proposed by Kubota et al. (1992), where the slip between the liquid and vapor interface is neglected and the liquid-vapor mixture is treated as a single fluid that satisfies the Navier–Stokes equations. A key point in this kind of model is how to define the mixture density. One approach is based on the state equation. Delannoy and Kueny (1990) used a barotropic state equation that linked the mixture density to the static pressure. Coutier-Delgosha et al. (2003) used a similar barotropic state equation together with a modified turbulent viscosity to successfully simulate cloud cavity shedding in a Venturi-type duct. Another model was a multiphase cavitation mixture model based on the transport equation for the phase change. Merkle et al. (1998) introduced an additional equation for the vapor (or liquid) volume fraction including source terms for evaporation and condensation (i.e. bubble growth and collapse). Kunz et al. (2000), Schnerr and Sauer (2001) and Singhal et al. (2002) used similar techniques with different source terms. There have been various comparative studies of the various cavitation models (Ducoin et al., 2012; Frikha et al., 2008; Morgut et al., 2011; Senocak and Shyy, 2004). Dular et al. (2007) numerically and experimentally investigated re-entrant jet reflection at an inclined cavity closure line around a hydrofoil with an asymmetric leading edge. Saito et al. (2007) investigated cavitating flows around a three dimensional hydrofoil with uniform profiles and uniform attack angles along the span wise direction and pointed out that the sidewall effect is the main reason for the generation of the U-shaped cavitation. Similarly, Yang et al. (2011) simulated unsteady cavitation shedding around a NACA66 hydrofoil with the sidewall effect and captured the crescent shaped cavity, which was due to the span wise pressure gradient. Most recently, an original formulation with a four-equation cavitation model was proposed to study isothermal cavitation (Goncalves and Charriere, 2014) and non-isothermal cavitation (Goncalvès, 2014). Their results show that for the periodic self-oscillating cavitation case, the new model reasonably simulated the sheet dynamics. The shedding two phase structures were more intense and in better agreement with the experimental data (Goncalves and Charriere, 2014). In addition, the four-equation cavitation model is also very attractive for studying thermodynamic effects and cryogenic cavitation (Goncalvès, 2014).

In cavitating flow simulations, the turbulence model is crucial because the cavitation is basically unsteady in nature and there are strong interactions between the cavity interface and the boundary layer during cavity development. Though the current Reynolds average Navier–Stokes (RANS) equation approach has been widely used to model turbulent flows in industry, the RANS models with eddy viscosity turbulence models have limited capability to simulate unsteady cavitating flows and need some modifications (Chen and Lu, 2008; Coutier-Delgosha et al., 2003; Decaix and Goncalves, 2013; Goncalves, 2011; Huang et al., 2013). Thus there have been attempts to predict the flow unsteadiness during cavitation using Large Eddy Simulation. LES models for cavitating flows are expected to give better predictions of larger-scale turbulent eddies with better accuracy with some promising results already obtained (Bensow and Bark, 2010; Dittakavi et al., 2010; Huang et al., 2014; Ji et al., 2013a; Luo et al., 2012; Roohi et al., 2013; Wang and Ostoja-Starzewski, 2007; Wosnik et al., 2006; Yu et al., 2014; Zhang and Khoo, 2013).

Although considerable research has been focused on the structure of the cavitating flow and its shedding dynamics, little attention has been given to the interaction between vortices and the cavities in turbulent cavitating flow. Gopalan and Katz (2000) demonstrated that the collapse of vapor cavities in the closure region is the primary vorticity production mechanism. Laberteaux and Ceccio (2001) further pointed out that baroclinic torques were responsible for the production of vorticity during vapor cloud collapse since density gradients within the cloud cavitation are not necessarily aligned with the pressure gradients around the cloud during collapse. In addition, the occurrence of sheet cavitation and the transition to cloud cavitation can result in very large unsteady loads on the cavitating objects. However,

few fundamental studies have examined this issue. Leroux et al. (2004) presented experimental results based on wall-pressure measurements with the aim of studying cavitation unsteadiness. They were able to demonstrate that the pressure at the hydrofoil surface during a cavity growth/destabilization cycle fluctuates dramatically.

The objective of the present paper is to investigate the effect of cavity growth and shedding on the dynamics of vortical flows by analyzing unsteady flows over a NACA66 hydrofoil. The LES approach was adopted to resolve time wise and space wise variation of the flow due to large scale eddies. An integrated one-dimensional/three-dimensional method was used to gain a better understanding of the complex physics involved in cavitation excited pressure fluctuation. This paper is organized as follows. A theoretical analysis of cavitation instability by a one-dimensional method is presented in Section 'Cavitation instability given by a one-dimensional analysis'. Mathematical formulations and numerical method of the CFD are described in Section 'Mathematical formulations and numerical method'. Detailed results and discussions are then given in Section 'Results and discussion' and the concluding remarks in Section 'Concluding remarks'.

Cavitation instability given by a one-dimensional analysis

To illustrate cavitation instability, consider a cavitating hydrofoil in a channel with area A, as shown in Fig. 1. A simplified one-dimensional model is used to analyze this configuration (Chen et al., 2008). A cavity with volume V_C is assumed on the suction side of the hydrofoil. Then, the continuity equation between the inlet and outlet flow rates (Q_1 and Q_2 respectively) is:

$$\widetilde{Q} = Q_2 - Q_1 = \frac{dV_C}{dt} \tag{1}$$

The inlet flow rate (Q_1) and the outlet pressure (p_{out}) are assumed to be constants. Applying the unsteady Bernoulli equation and neglecting the head loss in the channel, one can obtain,

$$p - p_{outlet} = \rho \frac{L_2}{A}\frac{dQ_2}{dt} = \rho \frac{L_2}{A}\frac{d\widetilde{Q}}{dt} \tag{2}$$

where L_2 is the length from the hydrofoil to the outlet, ρ is the density.

The classical cavitation compliance (C) can be defined as

$$C = -\frac{dV_C}{dp} \tag{3}$$

The cavitation compliance, firstly introduced by Brennen and Acosta (1976), is derived based on purely quasi-static considerations and does not involve any dynamic features of the cavity. Thus, the cavitation compliance is assumed not to be a function of time in the following stability analysis.

Using Eqs. (2) and (3), the continuity equation can be expressed as:

$$\widetilde{Q} = \frac{dV_C}{dt} = \frac{dV_C}{dp}\frac{dp}{dt} = -C\frac{dp}{dt} = -\rho C \frac{L_2}{A}\frac{d^2\widetilde{Q}}{dt^2} \tag{4}$$

Eq. (4) can be further written as

$$\frac{d^2\widetilde{Q}}{dt^2} + \frac{A}{\rho C L_2}\widetilde{Q} = 0 \tag{5}$$

This type of solution depends on the sign of the cavitation compliance C. For $C > 0$, this equation leads to periodic oscillations at the frequency:

$$\omega = \sqrt{\frac{A}{\rho C L_2}} \tag{6}$$

This case is typical of cavitation surge. The physical mechanism can be explained as follows (Franc and Michel, 2005). If $\widetilde{Q}$ is increased, Eq. (2) shows that the pressure at the location of the hydrofoil will increase. Then, the cavity volume V_C decreases due to the positive cavitation compliance ($C > 0$). From continuity (Eq. (1)), $\widetilde{Q}$ will be decreased. Hence, this situation is stable and auto-oscillations develop.

However, if $C < 0$, it will lead to exponential growth solutions and the results are not periodic and will be unstable. In fact, the cavity volume normally increases as the pressure decreases, so that the cavitation compliance is usually positive. Hence, the unstable behavior connected with negative values of the cavitation compliance is rather unusual (Franc and Michel, 2005).

Mathematical formulations and numerical method

The numerical simulation uses the LES method to solve the unsteady Navier–Stokes equations coupled with a mass transfer cavitation model. The main features of the solver are given below.

Physical cavitation model (Ji et al., 2013a)

The cavitation model used in this study was developed by Schnerr and Sauer (2001). The cavitation process is governed by the following mass transfer equation:

$$\frac{\partial(\rho_v \alpha_v)}{\partial t} + \frac{\partial(\rho_v \alpha_v u_j)}{\partial x_j} = \dot{m}^+ - \dot{m}^- \tag{7}$$

where α_v is the vapor volume fraction. The source terms $\dot{m}^+$ and $\dot{m}^-$ represent the effects of evaporation and condensation during the phase change and are derived from the bubble dynamics equation for the generalized Rayleigh–Plesset equation. They are defined as:

$$\dot{m}^+ = \frac{\rho_v \rho_l}{\rho}\alpha_v(1-\alpha_v)\frac{3}{R_b}\sqrt{\frac{2}{3}\frac{\max(p_v - p, 0)}{\rho_l}} \tag{8}$$

$$\dot{m}^- = \frac{\rho_v \rho_l}{\rho}\alpha_v(1-\alpha_v)\frac{3}{R_b}\sqrt{\frac{2}{3}\frac{\max(p - p_v, 0)}{\rho_l}} \tag{9}$$

The bubble radius is related to the vapor volume fraction, α_v, and the bubble number density, N_b, as:

$$R_b = \left(\frac{\alpha_v}{1-\alpha_v}\frac{3}{4\pi}\frac{1}{N_b}\right)^{1/3} \tag{10}$$

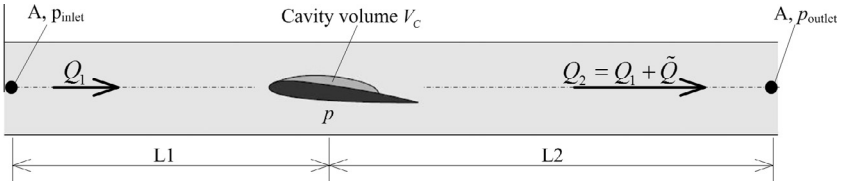

Fig. 1. Cavitating hydrofoil in a channel for the analysis.

where N_b is the only parameter which needs to be specified and is defined as 10^{13} according to Schnerr and Sauer (2001). This cavitation model has been validated for many cases, such as cavitating flow around a 2D hydrofoil (Li et al., 2010b) and a 3D hydrofoil (Li et al., 2010a).

Governing equations and the large-eddy simulation approach (Ji et al., 2013a)

In the mixture model for vapor/liquid two-phase flows, the multiphase fluid components are assumed to share the same velocity and pressure. The basic governing equations consist of the mass and momentum conservation equations,

$$\frac{\partial \rho}{\partial t}+\frac{\partial(\rho u_j)}{\partial x_j}=0 \tag{11}$$

$$\frac{\partial(\rho u_i)}{\partial t}+\frac{\partial(\rho u_i u_j)}{\partial x_j}=-\frac{\partial p}{\partial x_i}+\frac{\partial}{\partial x_j}\left(\mu\frac{\partial u_i}{\partial x_j}\right) \tag{12}$$

where u_i is the velocity in the i direction and p is the mixture pressure. The laminar viscosity, μ, and the mixture density, ρ, are defined as

$$\mu=\alpha_v\mu_v+(1-\alpha_v)\mu_l \tag{13}$$

$$\rho=\alpha_v\rho_v+(1-\alpha_v)\rho_l \tag{14}$$

Applying a Favre-filtering operation to Eqs. (11) and (12) gives the LES equations:

$$\frac{\partial \rho}{\partial t}+\frac{\partial(\rho \bar{u}_j)}{\partial x_j}=0 \tag{15}$$

$$\frac{\partial(\rho \bar{u}_i)}{\partial t}+\frac{\partial(\rho \bar{u}_i \bar{u}_j)}{\partial x_j}=-\frac{\partial \bar{p}}{\partial x_i}+\frac{\partial}{\partial x_j}\left(\mu\frac{\partial \bar{u}_i}{\partial x_j}\right)-\frac{\partial \tau_{ij}}{\partial x_j} \tag{16}$$

where the over-bars denote filtered quantities. Eq. (16) has an extra non-linear term that does not occur in Eq. (12):

$$\tau_{ij}=\rho(\overline{u_i u_j}-\overline{u_i}\,\overline{u_j}) \tag{17}$$

which are called the Sub-grid Scale (SGS) stresses and need to be modeled.

One commonly used SGS model is the eddy-viscosity model, which assumes that the SGS stresses are proportional to the modulus of the strain rate tensor, $\bar{S}_{ij}$, of the filtered large-scale flow,

$$\tau_{ij}-\frac{1}{3}\tau_{kk}\delta_{ij}=-2\mu_t\bar{S}_{ij} \tag{18}$$

where $\bar{S}_{ij}$ is the rate-of-strain tensor for the resolved scale and the sub-grid scale turbulent viscosity, μ_t, is closed by the LES Wall-Adapting Local Eddy-Viscosity (WALE) model (Nicoud and Ducros, 1999). The main advantages of the LES WALE model (Nicoud and Ducros, 1999) over the LES Smagorinsky model (Smagorinsky, 1963) are its ability to reproduce the laminar to turbulent transition and to return the correct wall-asymptotic y^{+3} – variation of the SGS model.

The sub-grid scale turbulent viscosity, μ_t, and the rate-of-strain tensor for the resolved scale, $\bar{S}_{ij}$, are modeled in the LES WALE model as (Nicoud and Ducros, 1999):

$$\mu_t=\rho L_s^2\frac{(S_{ij}^d S_{ij}^d)^{3/2}}{(\bar{S}_{ij}\bar{S}_{ij})^{5/2}+(S_{ij}^d S_{ij}^d)^{5/4}} \tag{19}$$

$$\bar{S}_{ij}=\frac{1}{2}\left(\frac{\partial \bar{u}_i}{\partial x_j}+\frac{\partial \bar{u}_j}{\partial x_i}\right) \tag{20}$$

$$S_{ij}^d=\frac{1}{2}\left(\bar{g}_{ij}^2+\bar{g}_{ji}^2\right)-\frac{1}{3}\delta_{ij}\bar{g}_{kk}^2,\ \bar{g}_{ij}=\frac{\partial \bar{u}_i}{\partial x_j},\ L_s=\min\left(kd,C_sV^{1/3}\right) \tag{21}$$

where L_s is the sub-grid scale mixing length, k is von Karman's constant, d is the distance to the closest wall, V is the volume of the computational cell and C_s is the WALE constant having the value of 0.5 based on calibrations using freely decaying isotropic homogeneous turbulence (Nicoud and Ducros, 1999).

Simulation setup

The time-dependent governing equations were discretized in both space and time domains. The high order resolution scheme (Barth and Jesperson, 1989) was used for the convective term, with the second order central difference scheme used for the diffusion term in the governing equations. The second-order implicit formulation was used for the transient term. The direct coupling method was used to solve the equations. The discrete continuity and momentum equations for the complete flow field were solved together without iterations and corrections. This solver strategy needs more computer storage, but improves the stability of the numerical procedure. The simulations were conducted using commercial CFD software.

The unsteady cavitating flow simulations were started from a steady non-cavitating flow field. The cavitation model and unsteady solver were then turned on for the cavitating flow simulations. The time step was set to 1.407×10^{-4} s ($T_{ref}/200$, where $T_{ref}=C/V_\infty$ and V_∞ is the inflow velocity at the domain inlet) (Coutier-Delgosha et al., 2003).

A NACA66 hydrofoil was used in the present research. The hydrofoil has a relative maximum thickness of 12% at 45% chord length from the leading edge and a relative maximum camber of 2% at 50% from the leading edge. The unsteady cavitation behavior around a NACA66 hydrofoil in a cavitation tunnel was extensively studied by Leroux et al. (2004). The hydrofoil chord length in the experiments was $C=0.15$ m and the foil was fixed within a 1 m long and 0.192 m wide square test section. The attack angle was 6 degrees. The inflow velocity was $V_\infty=5.33$ m/s and the static pressure was adjusted to vary the cavitation number, defined as:

$$\sigma=(p_{out}-p_v)/(0.5\rho_l V_\infty^2) \tag{22}$$

The computational domain is shown in Fig. 2. It is noted that it is difficult to use the real spanwise size of the experimental hydrofoil at present due to the requirement of very large computational resources. Thus, the spanwise length is chosen as 0.3C in present paper, as the spanwise domain is usually set as at least twice the thickness of the hydrofoil to resolve streamwise vortex (Sagaut, 2002). A periodic condition is used in the spanwise direction of the hydrofoil. This treatment is an effective way to investigate the fundamental turbulent-vortex interaction, as reported recently by many researchers (Chen et al., 2010b; Lakshmipathy and Girimaji, 2010). The hydrofoil was located in a channel having a height of 1.28C. The domain inlet was 2C upstream of the leading edge and the outlet was 6C downstream of the leading edge. The boundary conditions consisted of an imposed velocity at the inlet

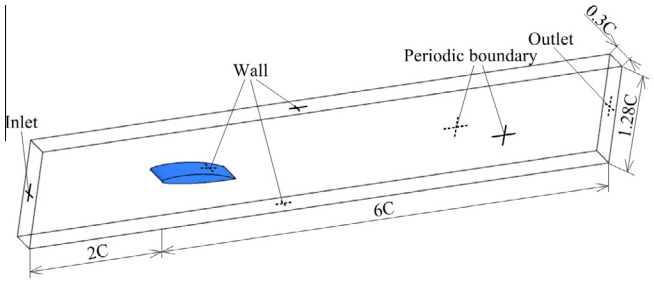

Fig. 2. Computational domain and boundary condition.

and a fixed static pressure at the outlet with free slip wall conditions at the upper and lower walls and non-slip walls on the hydrofoil. An O–H type grid was generated for the domain with sufficient refinement near the foil surface. It is noted that the values of y^+ calculated at the first grid point away from the hydrofoil surface were within 1–2. In present study, the investigation of mesh influence was performed by monitoring the lift and drag coefficients and cavitation shedding frequency, which was defined as follows:

$$C_L = \frac{Lift}{0.5\rho \times V_\infty^2 \times C \times Span} \quad C_D = \frac{Drag}{0.5\rho \times V_\infty^2 \times C \times Span} \quad St = \frac{f \times C}{V_\infty} \tag{23}$$

Three mesh resolutions were tested as shown in Table 1. The mesh distribution in mid-plane is the same for all three cases according to the mesh generation method in previous 2D hydrofoil research (Ji et al., 2013a,b). The only difference is the number of nodes in the spanwise direction, as shown in Fig. 3. From the results shown in Table 1, it is indicated that the differences between the medium and fine resolution meshes can be neglected. It should also be noted that any further grid refinement leads to relatively more complex vortical structures in the rear part of cavity wake as shown in Fig. 4, which will require more computational resources. This is not however the focus of this paper and is the subject of future work. Thus, case 2 (i.e. the medium resolution mesh) was selected as the final mesh, and the final grid nodes are about 2.5 million. On the other hand, the pressure fluctuation with a distance $x/C = 0.7$ from the leading edge of the hydrofoil suction surface is obtained after 6000 time steps calculation in Fig. 5(a). The corresponding power spectrum density (PSD) is shown in Fig. 5(b). The resolved scales seem to be asymptotic to an inertial subrange, reasonably close to $f^{-5/3}$ scaling. The spatial spectrum can be approximately obtained using Taylor's hypothesis which is limited to homogeneous turbulence with small turbulence intensity (Pope, 2000). The illustrated slope indicates that the present calculation may capture the turbulence spectrum. The primary frequency corresponding to the cavitation shedding events is $f = 3.667$ Hz approximately, which is quite close to the experimental value of $f = 3.625$ Hz.

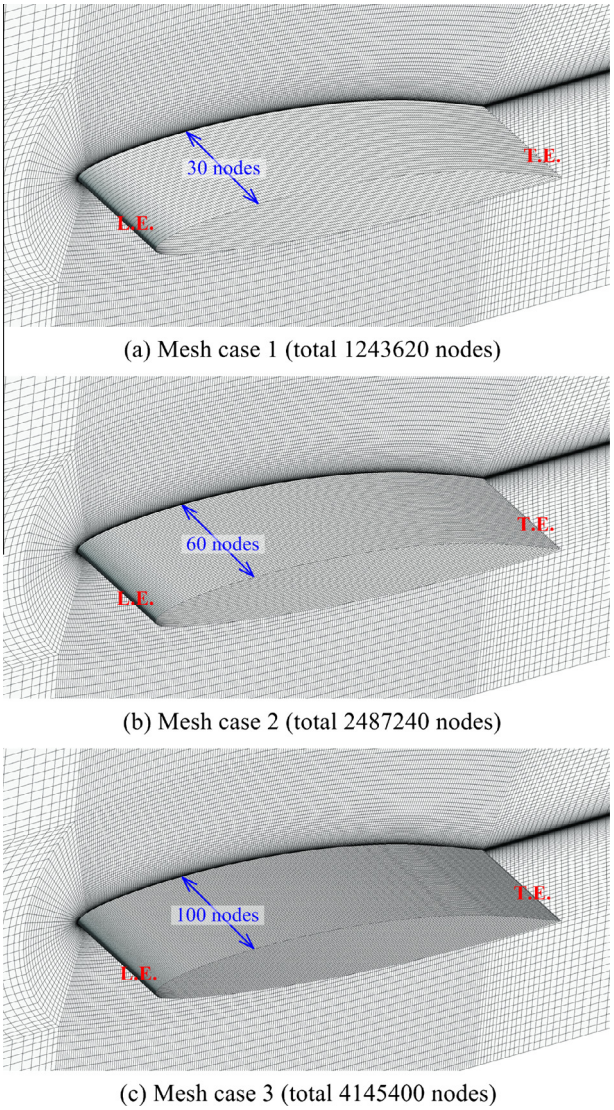

(a) Mesh case 1 (total 1243620 nodes)

(b) Mesh case 2 (total 2487240 nodes)

(c) Mesh case 3 (total 4145400 nodes)

Fig. 3. Three cases of mesh around the three dimensional hydrofoil surface.

Results and discussion

The simulations in the present paper aim to analyze sheet/cloud cavitation shedding dynamics. The numerical results are compared with available experimental data (Leroux et al., 2004) to analyze the typical partial cavitation transition mechanism.

Sheet/cloud cavitation structure and transient behavior

The experiments by Leroux et al. (2004) showed that when the cavity length was longer than half the foil chord ($\sigma \leqslant 1.25$), a cavity growth/destabilization cycle was observed with periodic shedding of vapor clouds. The sheet cavity grows and rolls up, and is then shed off and finally collapses. This process is quasi-periodic and its shedding frequency is about 3.625 Hz for cavitating flow around NACA66 hydrofoil at $\sigma = 1.25$ and $\alpha = 6°$ in the experiment. This type of sheet/cloud cavitation shedding is also shown in the numerical simulation. It should be noted that the cavitation number in the experiments (Leroux et al., 2004) is defined according to the upstream pressure, while the one in the simulation is based on the outlet pressure. In order to compare the numerical results with experiments, we adjust the outlet pressure properly until the time averaged inlet pressure corresponded to the experimental cavitation number.

To show the time evolution of cloud cavitation calculated by the present method, eight numerical snapshots with an interval of 0.04 s are shown in Fig. 6, where the predicted cavity shape is illustrated by the iso-surface of vapor volume fraction of 0.1. The corresponding instantaneous spanwise vorticity contours in the mid-plane are also shown in Fig. 6 to illustrate vortex evolution during cavitation shedding dynamics, where the lowest vorticity is shown in blue and the highest vorticity is shown in red. A negative vorticity represents fluid with counter-clockwise rotation if the main flow is from right to left (Fig. 6), while a positive vorticity means the fluid particles rotate in the clockwise direction. The corresponding experimental photos (Leroux et al., 2004) are shown at each time step in Fig. 7 to compare with the numerical results. The positions of the leading edge and trailing edge of the hydrofoil as well as flow direction are marked in those pictures.

Table 1
Results of the mesh independence test.

	Mesh resolution	Nodes	C_L	C_D	St = fC/V_∞
Case 1	Coarse	1,243,620	0.912	0.086	0.111
Case 2	Medium	2,487,240	0.922	0.087	0.103
Case 3	Fine	4,145,400	0.923	0.087	0.103
Exp.	–	–	–	–	0.102

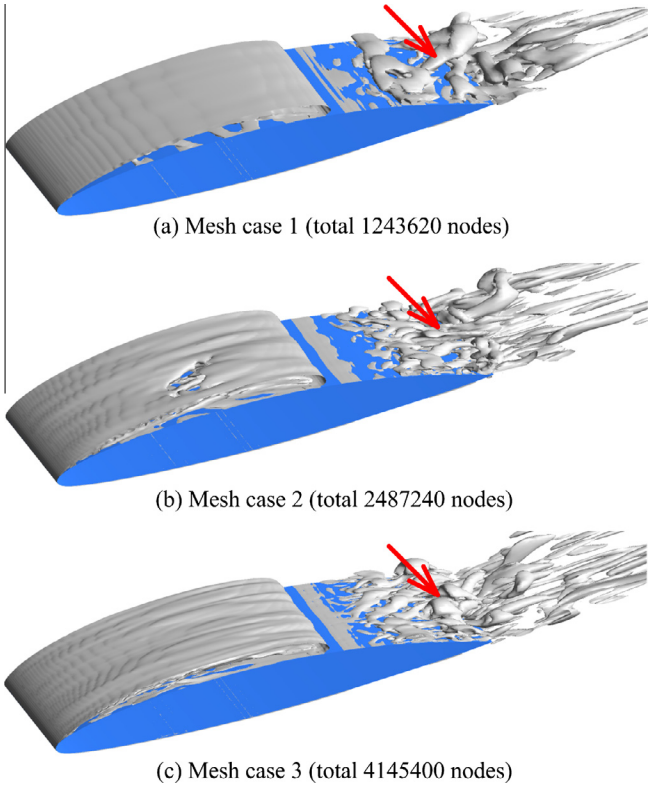

Fig. 4. Vortical structures by isosurface of the Q-criterion (Q = 50,000 [s^{-2}]).

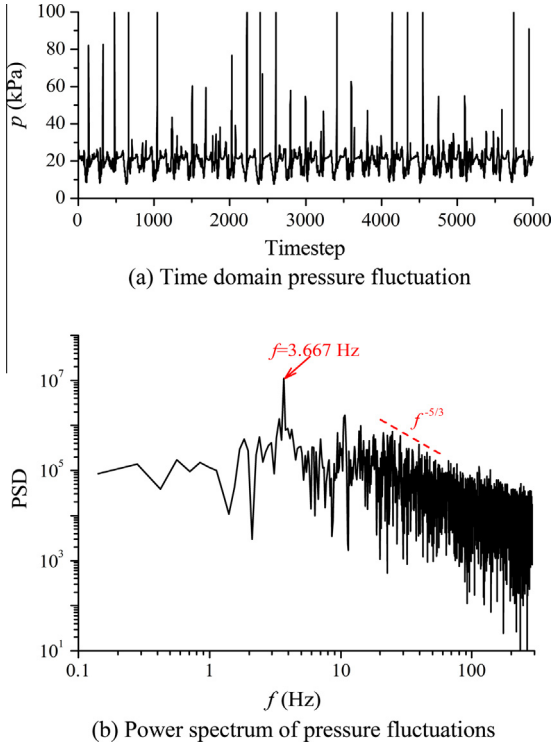

Fig. 5. The pressure fluctuation and PSD analysis at the point with x/C = 0.7 from the leading edge of the hydrofoil suction surface.

Good agreement between experiments and numerical simulations is observed. To better illustrate the unsteady behavior of transient cavitating flow, the total vapor volume calculated at each time step is shown in Fig. 8(a) with 6000 time-step unsteady calculations. The time axis in Fig. 8(b) was paneled in such a way that only part of numerical results (about two cycles) is shown to compare with the available experimental data of pressure fluctuations, and marked with 8 typical instants of time as shown in Fig. 6 and defined as:

$$V_c = \sum_{i=1}^{N} \alpha_i V_i \tag{24}$$

where N is the total number of control volumes in the computational domain, α_i is the vapor volume fraction in each control volume and V_i is the volume of each cell.

In Fig. 6(a)–(c), an attached cavity starting near the nose and extending to about 3/4 chord length position is apparently taking place. During this process, the attached cavity becomes thicker and a re-entrant flow develops towards the hydrofoil leading edge. After the re-entrant jet reaches the leading edge and collides with the cavity interface, a partial break-off ensues and a cloud gets organized at t = 0.314 s as shown in Fig. 9. A new leading edge cavity then begins to grow as indicated by Fig. 6(d) and (e). During this phase, shed cloud cavitation is further convected downstream. It should be noted that both numerical simulation and experimental observation have clearly demonstrated that the shedding cloud cavity has changed from a two dimensional smooth pocket of vapor into a highly turbulent vapor cloud with a three dimensional structure as shown in Figs. 6 and 7. Further on in the cycle, the cloud cavitation collapses downstream and the pressure at the rear of the attached cavity is increased, which causes the attached cavitation to quickly shrink as indicated in Fig. 6(g) and (h).

Cavitation-vortex interaction

From these results, it is shown that the transition of sheet cavitation to cloud cavitation can result in a highly unstable flow. In order to study cavitation-vortex interaction, the vorticity transport equation in a variable density flow is employed as follows,

$$\frac{D\vec{\omega}}{Dt} = (\vec{\omega}\cdot\nabla)\vec{V} - \vec{\omega}(\nabla\cdot\vec{V}) + \frac{\nabla\rho_m \times \nabla p}{\rho_m^2} + (\nu_m + \nu_t)\nabla^2\vec{\omega} \tag{25}$$

In this equation, the first term on the right hand side (RHS) is the vortex stretching term. This term represents the stretching and tilting of a vortex by velocity gradients. The second term on the RHS is the vortex dilatation term due to volumetric expansion/contraction, which describes how fluid compressibility affects the vorticity. The third term on the RHS is the baroclinic torque (due to misaligned pressure and density gradients). The last term on the RHS indicates the rate at which the vorticity changes due to viscous diffusion of the vorticity. Note that the viscous diffusion term has a much smaller effect on the vorticity transport than the other three terms in high Reynolds number flow (Huang et al., 2014; Ji et al., 2014).

Fig. 10 presents the predicted vapor volume fraction and contours of the vortex stretching, vortex dilatation and baroclinic torque terms in the mid-plane of hydrofoil at one typical cycle as shown in Fig. 6. These results are used to analyze the influences of the cavitation development on the turbulent vortical flows.

For t = 0.227 s (cavitation inception), the three terms give very different levels of vorticity transportation as shown in Fig. 10(a). The boundary layer is thin and the vorticity is mainly transported by vortex-stretching within the boundary shear layer, with the magnitudes shown in Fig. 10(a). The vortex dilatation and baroclinic torque terms are almost zero because the two terms of vortex dilatation and baroclinic torque in Eq. (25) are directly related to the velocity divergence, $\nabla\cdot V$, and the density gradient, $\nabla\rho$, which are both zero in the non-cavitating case (considered to be incompressible).

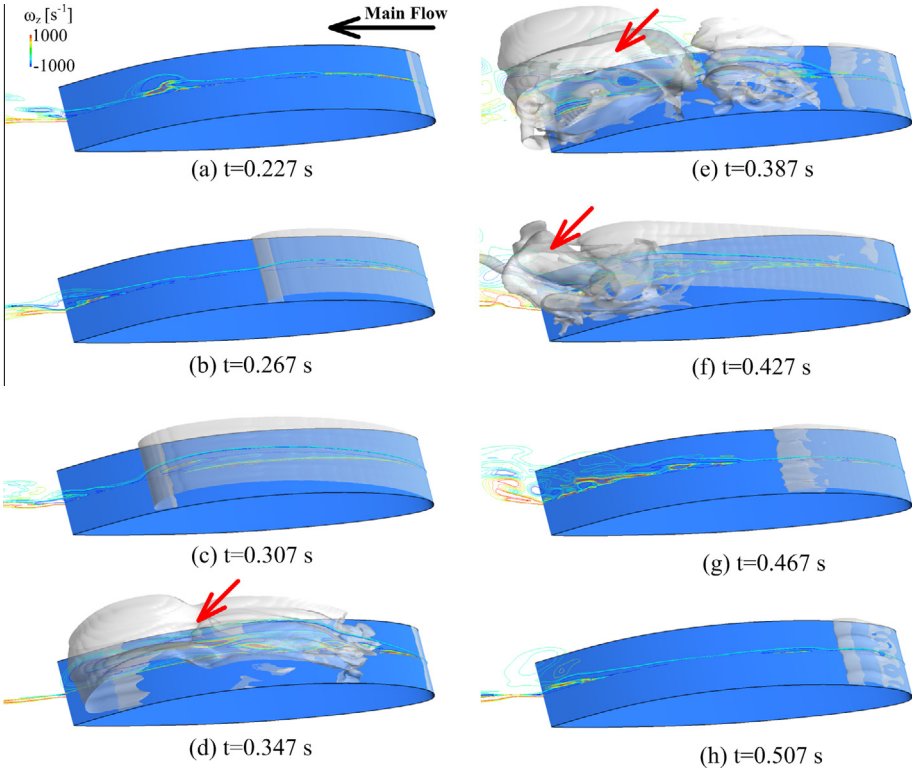

Fig. 6. Time evolution of calculated cavitation shedding in one typical cycle.

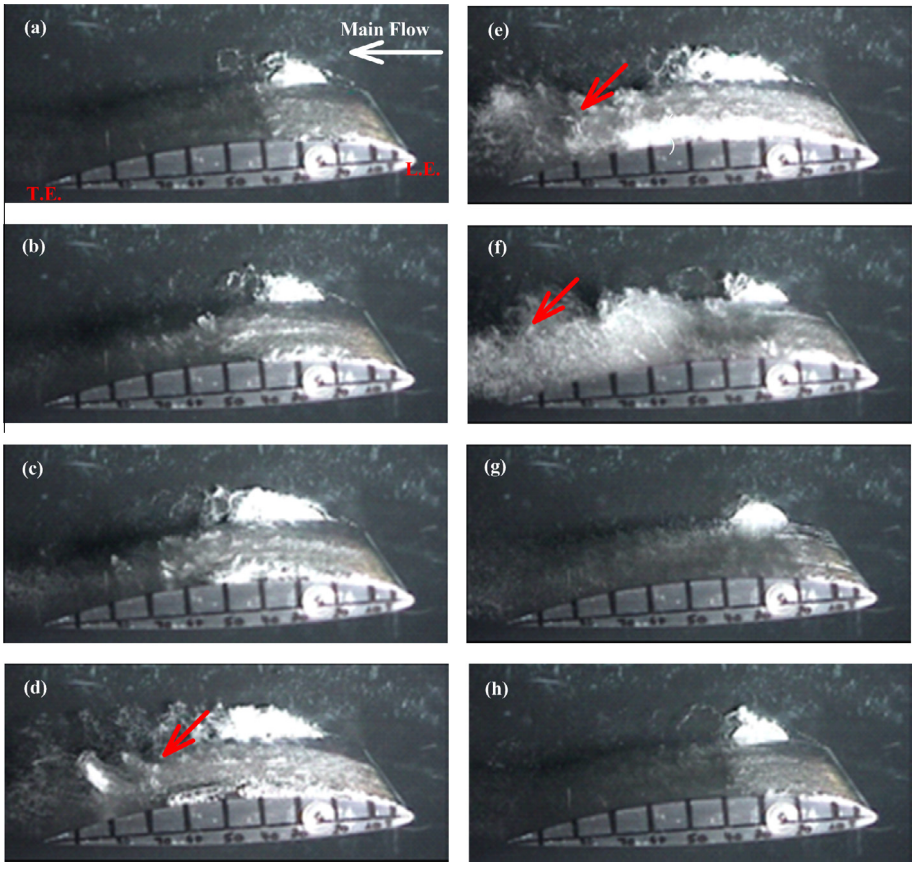

Fig. 7. Experimental observation of partial cavitation shedding in one typical cycle. Time between two consecutive images is 0.04 s (Leroux et al., 2004).

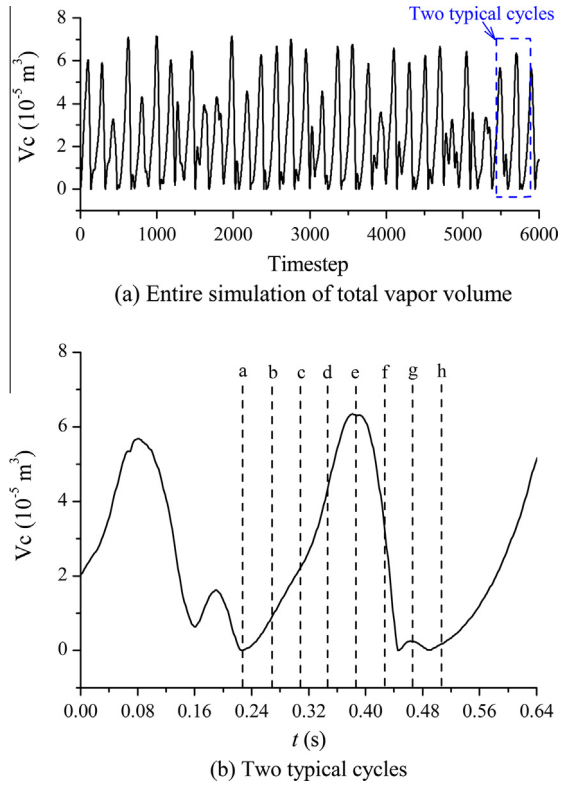

Fig. 8. Calculated total vapor volume.

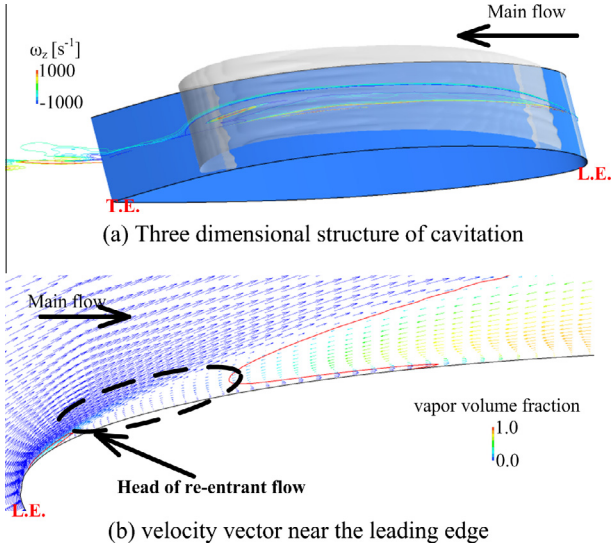

Fig. 9. Cavitation shedding at the instant of $t = 0.314$ (s).

For $t = 0.267$ s and $t = 0.307$ s (attached cavitation development), as explained earlier, a longer sheet cavitation appears and develops from the leading edge which increases the local boundary layer thickness of the hydrofoil. During this process, the attached cavitation increases in length and is filled with vortex structures. As indicated in Fig. 10(b) and (c), this vortex becomes considerably thicker than that in the cavitation inception case. Analysis of the flow field shows that the mass transfer along the cavity surface involves an increase in the vortex dilatation and baroclinic torque terms, which might be the main mechanism producing the cavitating vortex. For $t = 0.267$ s and $t = 0.307$ s, the baroclinic torque term is important along the liquid-vapor interface, but negligible inside the attached cavity region, especially when the cavity reaches its maximum at $t = 0.307$ s. The dilatation term represents volumetric expansion or contraction of a fluid element due to local density changes and is zero for the non-cavitation region. According to the experimental results of Leroux et al. (2004), relatively stable partial cavities appear with weak variations of the cavity closure interface and the liquid–vapor interface containing a series of eddies and massive cloud shedding does not yet occur at this stage

After the re-entrant jet reaches the head of attached cavitation (Fig. 9), cavitation shedding occurs and is rolled up into vortex structures from the leading edge. We often call this vortex structure as cloud cavitation. The cloud cavitation is then further convected downstream. It should be noted that the transition between a continuous sheet and cloud cavitation is highly unstable and the cloud cavitation is quickly changed from 2D to 3D structures. In order to illustrate the mechanism of this transition, the strengths of $(\vec{\omega}\cdot\nabla)\vec{V}$, $\vec{\omega}(\nabla\cdot\vec{V})$ and $(\nabla\rho_m\times\nabla p)/\rho_m^2$ are shown in Fig. 10(d)–(f) to show the influence of the cavitation on the vorticity production/variation from $t = 0.347$ s to $t = 0.427$ s. These figures show that there is strong correlation between the cloud cavitation and vorticity structures, which suggests that cavitation might be an important mechanism for vorticity generation. The results at $t = 0.347$ s and $t = 0.387$ s yield very high levels of the vortex stretching and dilatation terms if compared with that at $t = 0.267$ s and $t = 0.307$ s. These results demonstrate that there is strong vortex-cavitation interaction in the shedding vapor cloud and the vortex stretching and dilatation is the primary mechanism of the transition of cloud cavitation from 2D to 3D.

As the shedding vapor cloud collapses downstream, the attached cavity shrinks quickly and the evolution of the predicted three terms of the vorticity transport equation are shown in Fig. 10(g) and (h). During this process, the attached cavitation and boundary layer become very thin. The strength of the vortex stretching term and dilatation term decreased significantly along with the cavitation region. The cavitation structure then changes from 3D to 2D again. Even though the magnitude of the baroclinic torque term is smaller when compared with the vortex stretching term and dilatation term, the baroclinic torque is very important for the production of vorticity and modifies the vorticity field in regions with high density and pressure gradients, i.e. along the liquid–vapor interface and near the cavity closure.

Analysis of pressure fluctuation around the hydrofoil surface

Once cavity shedding occurs, the wall pressure along the hydrofoil surface varies greatly due to the dynamic behavior of cavitation. Numerical predictions of pressure fluctuations at three points, $x/C = 0.3$, 0.5, and 0.7 from the leading edge on the suction surface are plotted in Fig. 11 along with the experimental data (Leroux et al., 2004). As indicated from Figs. 6 and 11, the pressure at points $x/C = 0.3$, 0.5, and 0.7, drops to the vapor pressure in an orderly succession when these points were covered with sheet cavitation (from $t = 0.227$ s to $t = 0.307$ s). Comparison of the spatial-temporal pressure distributions on these points with experimental data shows that the sheet cavitation growth stage is well predicted, however some differences are noticeable. In present simulation, the period of the sheet cavitation growth is a little shorter than the experiment. Due to this, the predicted pressure signals at $x/C = 0.3$ and 0.7 are quite different from that of experimental results as indicated by the arrow line in Fig. 11. One possible reason of this disagreement is due to the fact that cavitation inception and development from the leading edge is initiated by the stream-wise vortex which is not resolved by present simulation. This tendency is also consistent with the recent simulation results using Large Eddy Simulation (Huang et al., 2014; Yu et al., 2014).

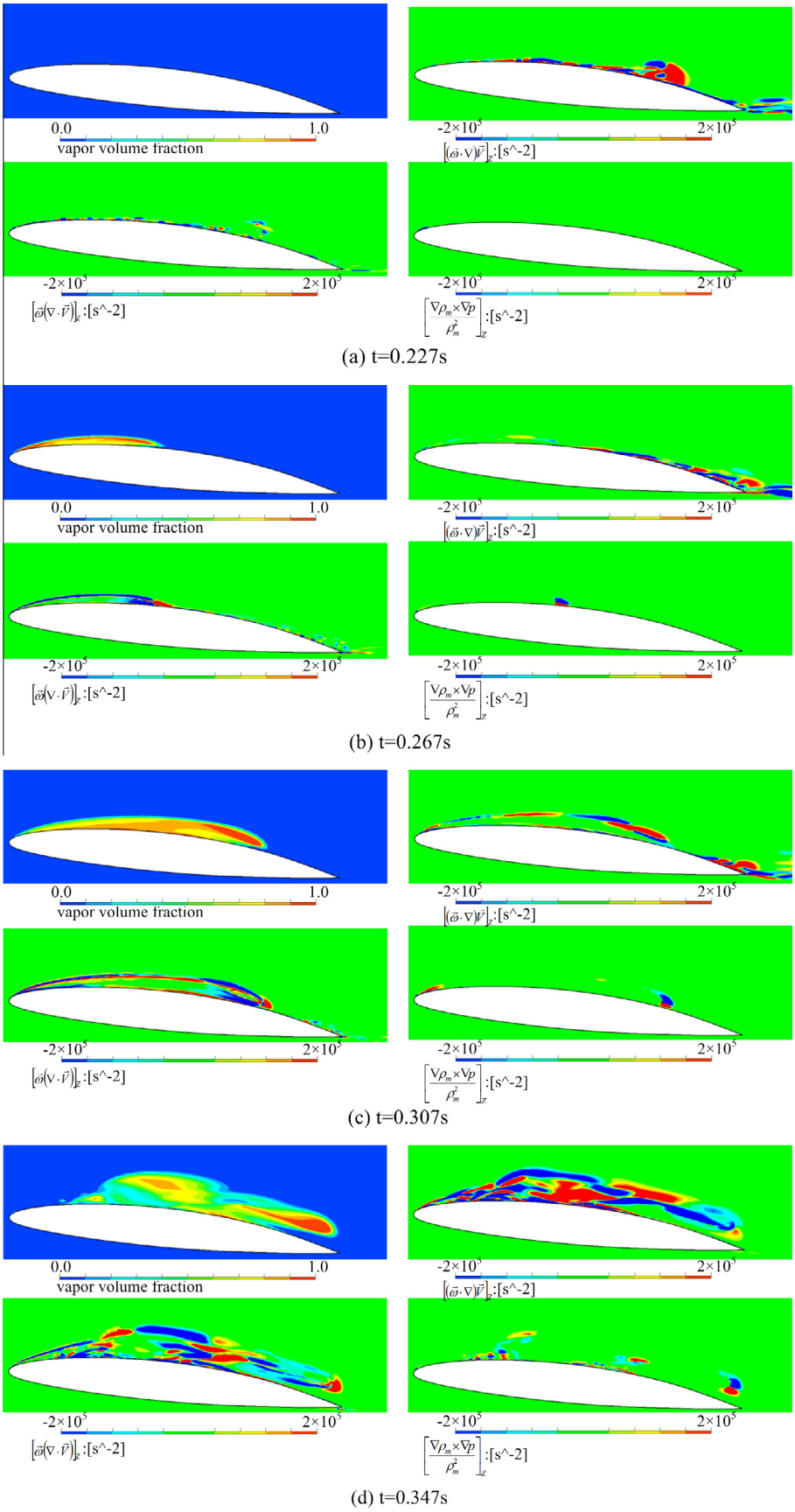

Fig. 10. The predicted vapor volume fraction, vortex stretching term, vortex dilatation term and baroclinic torque term.

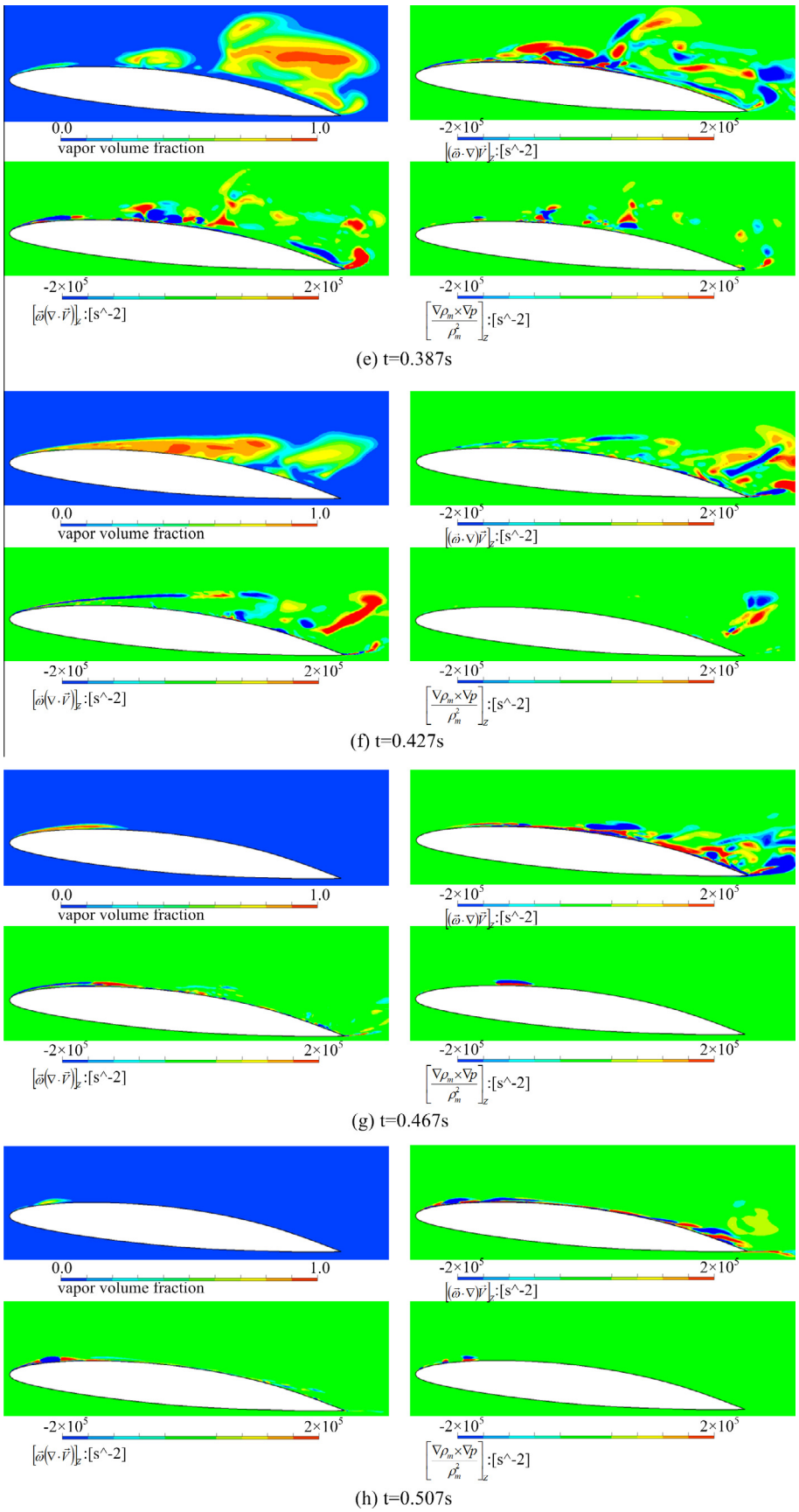

Fig. 10 (*continued*)

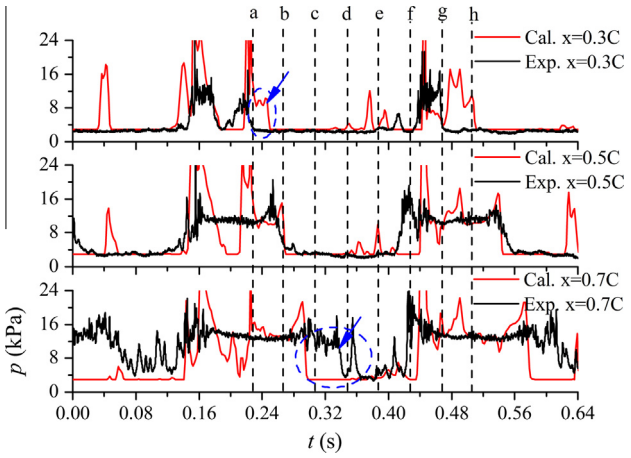

Fig. 11. Pressure fluctuation on suction surface of hydrofoil at $x = 0.3C$, $x = 0.5C$ and $x = 0.7C$.

The experimental observations (Leroux et al., 2004) indicated that at this stage the finger-shape leading edge cavitation caused by stream-wise vorticity is clearly visible, which was beyond the ability of present work to capture based on the assumption of homogeneous flow. Furthermore, it should be emphasized that the predicted pressure fluctuations, shown in Fig. 11 (from $t = 0.427$ s to $t = 0.467$ s), are much more violent and occur a little bit later on the points with $x/C = 0.5$ and 0.7 than those in the experiment.

It is also interesting to investigate pressure fluctuation on the pressure side of hydrofoil. Fig. 12 shows the pressure fluctuation at $x/C = 0.5$ on the pressure side. It is found that the present simulation over-predicts the magnitudes of fluctuations, which is also found by 2D simulation with a RANS solver (Seo and Lele, 2009; Zhang et al., 2014). It should be noticed that pressure fluctuations in Fig. 12 are plotted using different scales for a qualitative comparison with good agreement between the two signals in terms of both the period and the phase. Although the predicted pressure curve reflects the main features of the pressure fluctuation in Fig. 12 obtained in the experiment, the high frequency components of the pressure fluctuations in experiments are not well simulated. The reason for this may be due to the insufficient resolution of the bubble collapse (Zhang, 2013; Zhang and Li, 2014a,b), which is beyond the ability of the present model.

Analysis with the one-dimensional model

From above analysis, it is clearly indicated that the pressure fluctuation on the hydrofoil is highly correlated with the cavitation shedding dynamics. In order to better understand this mechanism, a simplified one-dimensional model for the present configuration is used and calibrated using the LES results. In the one-dimensional model, the continuity equation, Eq. (1), and the unsteady Bernoulli equation, Eq. (2), are combined to derive the characteristic equation, Eq. (5), for the cavitating hydrofoil system. The validity of the one-dimensional model is examined by comparing the result of the continuity and unsteady Bernoulli equation with the present LES results.

The difference between the upstream flow rate, Q_1 and downstream flow rate, Q_2, and the first derivative of the cavity volume, dV_C/dt, are plotted in Fig. 13. For the CFD boundary conditions used here, the upstream flow rate, Q_1, is fixed during the simulation and the cavitation on the hydrofoil will cause the outlet flow rate fluctuations. As indicated in Fig. 13, the flow rate difference, $Q_2 - Q_1$, matches very well with the first derivative of the cavity volume, dV_C/dt. Besides, it is noted that dV_C/dt underestimates the flow rate difference, $Q_2 - Q_1$, during the period from $t = 0.347$ s to $t = 0.427$ s as indicated in Fig. 13. This tendency was also reported by Chen et al. (2010a). According to the above discussion of flow structure, the shedding vapor cloud has experienced the transition from 2D to 3D during this period, which would be beyond the assumption of one-dimensional method.

The characteristic equation, Eq. (5), shows that the frequency of cavitation oscillations is determined by A and L_2. Since these factors can be traced back to the Bernoulli equation, Eq. (2) is evaluated by comparison with the simulation results. The results are compared at a point on the pressure side of the hydrofoil midplane with $x/C = 0.5$, named p05. The pressure side point is used instead of the suction side to avoid the effect of the cavity wake. Fig. 14

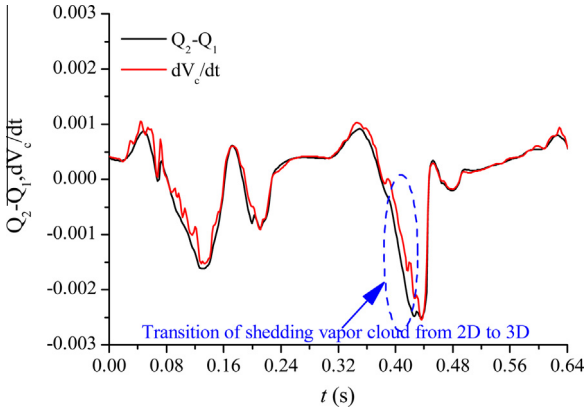

Fig. 13. Time dependent flow rate difference and cavity volume change rate.

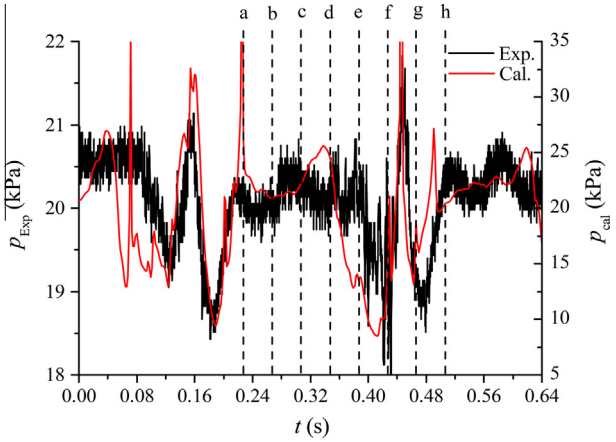

Fig. 12. Pressure fluctuation on pressure surface of hydrofoil at $x = 0.5C$.

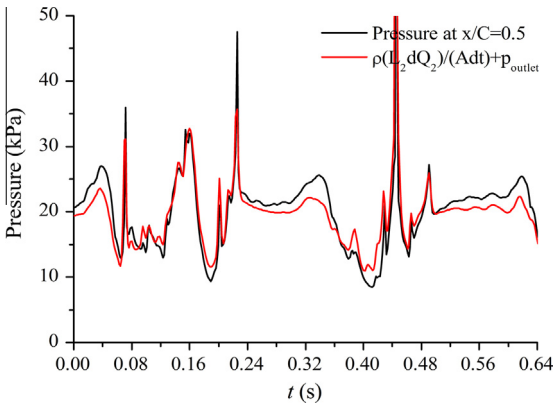

Fig. 14. Time dependent data of the terms in unsteady Bernoulli equation.

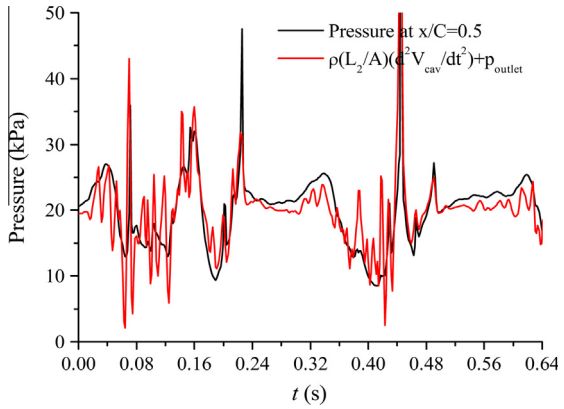

Fig. 15. Comparison of pressure fluctuations predicted by the one dimensional model and the CFD at p05.

shows the pressure fluctuations predicted by the LES at p05 and pressure fluctuations estimated by Eq. (2). Here L_2 and A are equal to $5.5C$ and $0.384C^2$, where C is the hydrofoil chord length with the value of 0.15 m. The agreement between these two curves indicates that the expression in Eq. (2) can effectively predict the pressure pulsations.

Further insight into cavitation excited pressure fluctuation

The mechanism for the pressure fluctuations being excited by the cavitation shedding can be seen by relating the cavitation evolution and the pressure fluctuations.

The one-dimensional model is used to illustrate this mechanism in detail. Combining Eqs. (1) and (2) gives:

$$p - p_{\text{outlet}} = \rho \frac{L_2}{A} \frac{d^2 V_C}{dt^2} \tag{26}$$

This shows that the pressure fluctuation around the cavitating hydrofoil is proportional to the second derivative of cavity volume, also named the cavity volume acceleration.

The calculated total vapor volume, V_c, was obtained from the CFD results using Eq. (24) in each time step. The cavity volume data was then smoothed and used to determine the second derivative of the cavity volume and, therefore, the volumetric acceleration imposed upon the flow. Then the pressure pulsation was calculated using Eq. (26). Fig. 15 compares the pressure fluctuations calculated by one dimensional model and those from the CFD results for point p05 with good agreement between the two signals in terms of both the period and the phase. Thus, the one dimensional model accurately tracks the main features of the time-dependent pressure fluctuations.

Concluding remarks

Numerical simulation of the unsteady cavitating turbulent flow around a NACA66 hydrofoil was carried out by means of a Large Eddy Simulation (LES) coupled with a homogeneous cavitation model. Various fundamental mechanisms dictating the complex flow behaviors, including the cavitation shedding dynamics evolution, cavitation-vortex interaction and cavitation excited pressure fluctuation, were examined and summarized.

The predicted cavitation shedding dynamics behavior, including the cavity growth, break-off and collapse downstream, agrees fairly well with the experimental observations. In particular, both numerical simulation and experimental observation have clearly demonstrated that the shed cloud cavity has changed from a two dimensional smooth pocket of vapor into a highly turbulent vapor cloud with a three dimensional structure. The complicated vortex structure around the cavitating hydrofoil has been analyzed using the vorticity transport equation. Several observations are as follows:

(i) At the instant of cavitation inception, the boundary layer is thin and the vorticity is mainly transported by vortex-stretching within the boundary shear layer. The vortex dilatation and baroclinic torque terms are almost zero because the two terms of vortex dilatation and baroclinic torque are directly related to the velocity divergence and the density gradient, which are both zero in the incompressible non-cavitating case.

(ii) As the attached cavitation grows, a longer sheet cavitation appears and develops from the leading edge which increases the local boundary layer thickness of the hydrofoil. Analysis of the flow field shows that the mass transfer along the cavity surface involves an increase in the vortex dilatation and baroclinic torque terms, which might be the main mechanism producing the cavitating vortex. In addition, the baroclinic torque term is important along the liquid-vapor interface, but negligible inside the attached cavity region, especially when the cavity reaches its maximum. (iii) After the re-entrant jet reaches the head of attached cavitation, cavitation shedding occurs and is rolled up into vortex structures from the leading edge. Further analysis demonstrates that there is strong vortex-cavitation interaction in the shedding vapor cloud and the vortex stretching and dilatation is the primary mechanism of the transition of cloud cavitation from 2D to 3D.

(iii) As the shed vapor cloud collapses downstream, the attached cavity shrinks quickly and changes from 3D to 2D again. During this process, the attached cavitation and boundary layer become very thin. The strength of the vortex stretching term and dilatation term decreases significantly along with the extent of the cavitation region. Even though the magnitude of the baroclinic torque term is smaller if compared with the vortex stretching term and dilatation term, the baroclinic torque is very important for the production of vorticity and modifies the vorticity field in regions with high density and pressure gradients, i.e. along the liquid–vapor interface and near the cavity closure.

(iv) Pressure fluctuations along the hydrofoil surface, which are excited by periodic cavitation shedding dynamics, was simulated and compared with the available experimental data. The results showed that the present method can reasonably predict pressure oscillations on the suction surface of the hydrofoil, while that for the hydrofoil pressure side are overestimated.

(v) A simplified one-dimensional model for the present configuration is proposed and calibrated against the LES results. The results verify the relationship between the pressure fluctuations and the cavity shedding process (e.g. the variations of the flow rate and cavity volume) and demonstrate that the cavity volume acceleration is the main source of the pressure fluctuations around the cavitating hydrofoil. These results are essential for understanding the mechanism of the cavitation excited pressure pulsations, which will help development of engineering designs to control these oscillations.

Acknowledgements

This work was financially supported by the National Natural Science Foundation of China (Project Nos. 51206087, 51179091 and 11332009), the National Science & Technology Pillar Program

during the Twelfth Five-Year Plan Period (Project No. 2011BAF03B01), and the China Postdoctoral Science Foundation funded Projects (2011M500314 and 2012T50090).

References

Arndt, R.E.A., 1981. Cavitation in fluid machinery and hydraulic structures. Annu. Rev. Fluid Mech. 13, 273–328.

Arndt, R.E.A., 2002. Cavitation in vortical flows. Annu. Rev. Fluid Mech. 34, 143–175.

Arndt, R.E.A., Song, C.C.S., Kjeldsen, M., Keller, A., 2000. Instability of partial cavitation: a numerical/experimental approach. In: Proceedings of the Twenty-Third Symposium on Naval Hydrodynamics, Val de Reuil, France.

Astolfi, J.A., Dorange, P., Billard, J.Y., Tomas, I.C., 2000. An experimental investigation of cavitation inception and development on a two-dimensional Eppler Hydrofoil. J. Fluids Eng. 122, 164–173.

Barre, S., Rolland, J., Boitel, G., Goncalves, E., Patella, R.F., 2009. Experiments and modeling of cavitating flows in venturi: attached sheet cavitation. Eur. J. Mech. B-Fluid 28, 444–464.

Barth, T.J., Jesperson, D.C., 1989. The design and application of upwind schemes on unstructured meshes. In: 27th Aerospace Sciences Meeting, Reno, Nevada.

Bensow, R.E., Bark, G., 2010. Implicit LES predictions of the cavitating flow on a propeller. J. Fluids Eng. 132, 041302.

Brennen, C.E., 1995. Cavitation and Bubble Dynamics. Oxford University Press, New York.

Brennen, C., Acosta, A.J., 1976. The dynamic transfer function for a cavitating inducer. J. Fluids Eng. 98, 182–191.

Callenaere, M., Franc, J.P., Michel, J.M., Riondet, M., 2001. The cavitation instability induced by the development of a re-entrant jet. J. Fluid Mech. 444, 223–256.

Chen, Y., Lu, C.J., 2008. A homogenous-equilibrium-model based numerical code for cavitation flows and evaluation by computation cases. J. Hydrodyn. 20, 186–194.

Chen, C.K., Nicolet, C., Yonezawa, K., Farhat, M., Avellan, F., Tsujimoto, Y., 2008. One-dimensional analysis of full load draft tube surge. J. Fluids Eng. 130, 041106.

Chen, C.K., Nicolet, C., Yonezawa, K., Farhat, M., Avellan, F., Miyagawa, K., Tsujimoto, Y., 2010a. Experimental study and numerical simulation of cavity oscillation in a conical diffuser. Int. J. Fluid Mach. Syst. 3, 91–101.

Chen, L.W., Xu, C.Y., Lu, X.Y., 2010b. Numerical investigation of the compressible flow past an aerofoil. J. Fluid Mech. 643, 97–126.

Coutier-Delgosha, O., Reboud, J.L., Delannoy, Y., 2003. Numerical simulation of the unsteady behaviour of cavitating flows. Int. J. Numer. Methods Fluids 42, 527–548.

Decaix, J., Goncalves, E., 2013. Compressible effects modeling in turbulent cavitating flows. Eur. J. Mech. B-Fluid 39, 11–31.

Delannoy, Y., Kueny, J.L., 1990. Two Phase Flow Approach in Unsteady Cavitation Modeling. ASME Fluids Engineering Division, Toronto, Ontario, pp. 153–158.

Dittakavi, N., Chunekar, A., Frankel, S., 2010. Large Eddy Simulation of turbulent-cavitation interactions in a venturi nozzle. J. Fluids Eng. 132, 121301.

Ducoin, A., Huang, B.A., Young, Y.L., 2012. Numerical modeling of unsteady cavitating flows around a stationary hydrofoil. Int. J. Rotating Mach. Article ID 215678.

Dular, M., Bachert, R., Schaad, C., Stoffel, B., 2007. Investigation of a re-entrant jet reflection at an inclined cavity closure line. Eur. J. Mech. B-Fluid 26, 688–705.

Foeth, E.J., 2008. The Structure of Three-Dimensional Sheet Cavitation, Mechanical Maritime and Materials Engineering. Delft University of Technology, Wageningen, the Netherlands.

Foeth, E.J., van Doorne, C.W.H., van Terwisga, T., Wieneke, B., 2006. Time resolved PIV and flow visualization of 3d sheet cavitation. Exp. Fluids 40, 503–513.

Foeth, E.J., van Terwisga, T., van Doorne, C., 2008. On the collapse structure of an attached cavity on a three-dimensional hydrofoil. J. Fluids Eng. 130, 071303.

Franc, J.P., Michel, J.M., 2005. Fundamentals of Cavitation. Springer, Netherlands.

Frikha, S., Coutier-Delgosha, O., Astolfi, J.A., 2008. Influence of the cavitation model on the simulation of cloud cavitation on 2D foil section. Int. J. Rotating Mach. 2008, 146234.

Goncalves, E., 2011. Numerical study of unsteady turbulent cavitating flows. Eur. J. Mech. B-Fluid 30, 26–40.

Goncalvès, E., 2014. Modeling for non isothermal cavitation using 4-equation models. Int. J. Heat Mass Transfer 76, 247–262.

Goncalves, E., Charriere, B., 2014. Modelling for isothermal cavitation with a four-equation model. Int. J. Multiphase Flow 59, 54–72.

Gopalan, S., Katz, J., 2000. Flow structure and modeling issues in the closure region of attached cavitation. Phys. Fluids 12, 895–911.

Huang, B., Young, Y.L., Wang, G.Y., Shyy, W., 2013. Combined experimental and computational investigation of unsteady structure of sheet/cloud cavitation. J. Fluids Eng. 135, 071301.

Huang, B., Zhao, Y., Wang, G.Y., 2014. Large Eddy Simulation of turbulent vortex-cavitation interactions in transient sheet/cloud cavitating flows. Comput. Fluids 92, 113–124.

Ji, B., Luo, X.W., Peng, X.X., Wu, Y.L., 2013a. Three-dimensional large eddy simulation and vorticity analysis of unsteady cavitating flow around a twisted hydrofoil. J. Hydrodyn. 25, 510–519.

Ji, B., Luo, X.W., Wu, Y.L., Peng, X.X., Duan, Y.L., 2013b. Numerical analysis of unsteady cavitating turbulent flow and shedding horse-shoe vortex structure around a twisted hydrofoil. Int. J. Multiphase Flow 51, 33–43.

Ji, B., Luo, X.W., Arndt, R.E.A., Wu, Y.L., 2014. Numerical simulation of three dimensional cavitation shedding dynamics with special emphasis on cavitation–vortex interaction. Ocean Eng. 87, 64–77.

Kawanami, Y., Kato, H., Yamaguchi, H., Tanimura, M., Tagaya, Y., 1997. Mechanism and control of cloud cavitation. J. Fluids Eng. 119, 788–794.

Kravtsova, A.Y., Markovich, D.M., Pervunin, K.S., Timoshevskiy, M.V., Hanjalić, K., 2014. High-speed visualization and PIV measurements of cavitating flows around a semi-circular leading-edge flat plate and NACA0015 hydrofoil. Int. J. Multiphase Flow 60, 119–134.

Kubota, A., Kato, H., Yamaguchi, H., Maeda, M., 1989. Unsteady structure measurement of cloud cavitation on a foil section using conditional sampling technique. J. Fluids Eng. 111, 204–210.

Kubota, A., Kato, H., Yamaguchi, H., 1992. A new modeling of cavitating flows – a numerical study of unsteady cavitation on a hydrofoil section. J. Fluid Mech. 240, 59–96.

Kunz, R.F., Boger, D.A., Stinebring, D.R., Chyczewski, T.S., Lindau, J.W., Gibeling, H.J., Venkateswaran, S., Govindan, T.R., 2000. A preconditioned Navier–Stokes method for two-phase flows with application to cavitation prediction. Comput. Fluids 29, 849–875.

Laberteaux, K.R., Ceccio, S.L., 2001. Partial cavity flows. Part 1. Cavities forming on models without spanwise variation. J. Fluid Mech. 431, 1–41.

Lakshmipathy, S., Girimaji, S.S., 2010. Partially Averaged Navier–Stokes (PANS) method for turbulence simulations: flow past a circular cylinder. J. Fluids Eng. 132, 121202.

Le, Q., Franc, J.P., Michel, J.M., 1993. Partial cavities – global behavior and mean pressure distribution. J. Fluids Eng. 115, 243–248.

Leroux, J.B., Astolfi, J.A., Billard, J.Y., 2004. An experimental study of unsteady partial cavitation. J. Fluids Eng. 126, 94–101.

Li, D.Q., Grekula, M., Lindell, P., 2010a. Towards numerical prediction of unsteady sheet cavitation on hydrofoils. J. Hydrodyn. 22, 741–746.

Li, Z.R., Pourquie, M., van Terwisga, T., 2010b. A numerical study of steady and unsteady cavitation on a 2D hydrofoil. J. Hydrodyn. 22, 770–777.

Luo, X.W., Ji, B., Peng, X.X., Xu, H.Y., Nishi, M., 2012. Numerical simulation of cavity shedding from a three-dimensional twisted hydrofoil and induced pressure fluctuation by large-eddy simulation. J. Fluids Eng. 134, 041202.

Merkle, C.L., Feng, J.Z., Buelow, P.E., 1998. Computational modeling of the dynamics of sheet cavitation. In: Proceedings of the Third International Symposium on Cavitation, Grenoble, France.

Morgut, M., Nobile, E., Bilus, I., 2011. Comparison of mass transfer models for the numerical prediction of sheet cavitation around a hydrofoil. Int. J. Multiphase Flow 37, 620–626.

Nicoud, F., Ducros, F., 1999. Subgrid-scale stress modelling based on the square of the velocity gradient tensor. Flow Turbul. Combust. 62, 183–200.

Park, S., Rhee, S.H., 2013. Numerical analysis of the three-dimensional cloud cavitating flow around a twisted hydrofoil. Fluid Dyn. Res. 45, 015502.

Pham, T.M., Larrarte, F., Fruman, D.H., 1999. Investigation of unsteady sheet cavitation and cloud cavitation mechanisms. J. Fluids Eng. 121, 289–296.

Pope, S.B., 2000. Turbulent Flows. Cambridge University Press.

Reisman, G.E., Wang, Y.C., Brennen, C.E., 1998. Observations of shock waves in cloud cavitation. J. Fluid Mech. 355, 255–283.

Roohi, E., Zahiri, A.P., Passandideh-Fard, M., 2013. Numerical simulation of cavitation around a two-dimensional hydrofoil using VOF method and LES turbulence model. Appl. Math. Model. 37, 6469–6488.

Sagaut, P., 2002. Large Eddy Simulation for Incompressible Flows. Springer.

Saito, Y., Takami, R., Nakamori, I., Ikohagi, T., 2007. Numerical analysis of unsteady behavior of cloud cavitation around a NACA0015 foil. Comput. Mech. 40, 85–96.

Schnerr, G.H., Sauer, J., 2001. Physical and numerical modeling of unsteady cavitation dynamics. In: Proceedings of 4th International Conference on Multiphase Flow, New Orleans, USA.

Senocak, I., Shyy, W., 2004. Interfacial dynamics-based modelling of turbulent cavitating flows, Part-1: model development and steady-state computations. Int. J. Numer. Methods Fluids 44, 975–995.

Seo, J.H., Lele, S.K., 2009. Numerical investigation of cloud cavitation and cavitation noise on a hydrofoil section. In: Proceedings of the 7th International Symposium on Cavitation, Michigan, USA.

Singhal, A.K., Athavale, M.M., Li, H.Y., Jiang, Y., 2002. Mathematical basis and validation of the full cavitation model. J. Fluids Eng. 124, 617–624.

Smagorinsky, J., 1963. General circulation experiments with the primitive equations. Mon. Weather Rev. 91, 99–164.

Stutz, B., Reboud, J.L., 1997a. Experiments on unsteady cavitation. Exp. Fluids 22, 191–198.

Stutz, B., Reboud, J.L., 1997b. Two-phase flow structure of sheet cavitation. Phys. Fluids 9, 3678–3686.

Tassin, A.L., Li, C.Y., Ceccio, S.L., Bernal, L.P., 1995. Velocity field measurements of cavitating flows. Exp. Fluids 20, 125–130.

Wang, G., Ostoja-Starzewski, M., 2007. Large Eddy Simulation of a sheet/cloud cavitation on a NACA0015 hydrofoil. Appl. Math. Model. 31, 417–447.

Wang, G.Y., Senocak, I., Shyy, W., Ikohagi, T., Cao, S.L., 2001. Dynamics of attached turbulent cavitating flows. Prog. Aerosp. Sci. 37, 551–581.

Watanabe, S., Tsujimoto, Y., Furukawa, A., 2001. Theoretical analysis of transitional and partial cavity instabilities. J. Fluids Eng. 123, 692–697.

Wosnik, M., Qin, Q., Arndt, R.E.A., 2006. Identification of large scale structures in the wake of cavitating hydrofoils using LES and time-resolved PIV. In: Proceedings of the 6th International Symposium on Cavitation, Wageningen, The Netherland.

Yang, J., Zhou, L.J., Wang, Z.W., 2011. Numerical simulation of three-dimensional cavitation around a hydrofoil. J. Fluids Eng. 133, 081301.
Yu, X.X., Huang, C.G., Du, T.Z., Liao, L.J., Wu, X.C., Zheng, Z., Wang, Y.W., 2014. Study of characteristics of cloud cavity around axisymmetric projectile by large eddy simulation. J. Fluids Eng. 136, 051303.
Zhang, Y.N., 2013. A generalized equation for scattering cross section of spherical gas bubbles oscillating in liquids under acoustic excitation. J. Fluids Eng. 135, 091301.
Zhang, L.X., Khoo, B.C., 2013. Computations of partial and super cavitating flows using implicit pressure-based algorithm (IPA). Comput. Fluids 73, 1–9.
Zhang, Y.N., Li, S.C., 2014a. Mass transfer during radial oscillations of gas bubbles in viscoelastic mediums under acoustic excitation. Int. J. Heat Mass Transfer 69, 106–116.
Zhang, Y.N., Li, S.C., 2014b. Thermal effects on nonlinear radial oscillations of gas bubbles in liquids under acoustic excitation. Int. Commun. Heat Mass Transfer 53, 43–49.
Zhang, X.B., Zhang, W., Chen, J.Y., Qiu, L.M., Sun, D.M., 2014. Validation of dynamic cavitation model for unsteady cavitating flow on NACA66. Sci. China Technol. Sc 57, 819–827.